Moiré Superstructure-Dependent Growth Mechanisms of Transition Metal Dichalcogenides on the Au(111) surface

Xuan Wang,[a] Xuefeng Liang,[a] Haonan Pei,[a] Jichen Dong,*[b] Leining Zhang*[a]

[a] Key Laboratory of Cluster Science, Ministry of Education of China, Beijing Key Laboratory of Photoelectronic/Electrophonic Conversion Materials, School of Chemistry and Chemical Engineering, Beijing Institute of Technology Beijing100081, People's Republic of China.

*Email: leiningzhang@bit.edu.cn

[b] Beijing National Laboratory for Molecular Sciences, Key Laboratory of Organic Solids, Institute of Chemistry Chinese Academy of Sciences, Beijing 100190, People's Republic of China, E-mail: dongjichen@iccas.ac.cn

*Email: dongjichen@iccas.ac.cn

CONTENTS

I. Models for calculating edge formation energies

To determine the most stable configurations, we systematically calculated the formation energies of various MoS_2 edges. Unlike graphene, MoS_2 possesses two distinct zigzag (ZZ) edge types, making it impossible to obtain both S edge and Mo edge formation energies using solely ZZ-oriented nanoribbons. Therefore, we developed an approach combining triangular clusters (with single ZZ edge type) and nanoribbon structures.

1. In vacuum:

1.1 Two sized triangular clusters with pristine Mo edges were constructed (Figure S1):

$$E_{Mo\ edge} = \frac{E_1 - E_2 - \Delta N_{Mo}\mu_{Mo} - \Delta N_S\mu_S}{3(l_1 - l_2)} \#(1)$$

where E_1/E_2 are total energies, $\Delta N_{Mo}/\Delta N_S$ denote atom number differences, μ_{Mo}/μ_s are chemical potentials, which satisfy $2\mu_s+\mu_{Mo} = {}^{\varepsilon_{MoS_2}}2$, where ${}^{\varepsilon_{MoS_2}}2$ is the energy of a MoS_2 pair in a MoS_2 monolayer sheet, and l_1/l_2 are side lengths.

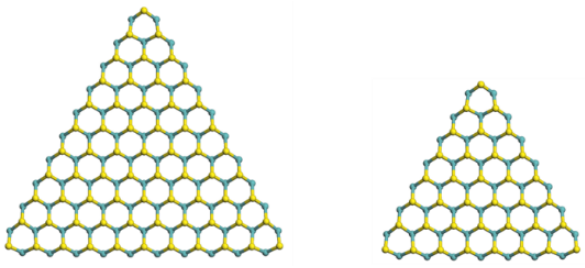

Figure S1. Two optimized triangular MoS_2 domains with only raw Mo edge.

1.2 Nanoribbons containing pristine ZZ-Mo edge and ZZ-S edges were built (such as Figure S2) to calculate the formation energy of reconstructed ZZ-S edges:

$$E_{S\,edge} = \frac{E_0 - \Delta N_{Mo}\mu_{Mo} - \Delta N_S\mu_S - E_{Mo\,edge} \times L}{L} \#(2)$$

where E_0 is nanoribbon energy, L is the length of nanoribbons, and $E_{Mo\,edge}$ is formation energy of ZZ-Mo edge.

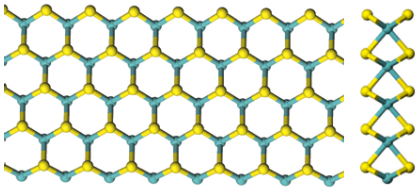

Figure S2. The optimized nanoribbon with pristine ZZ-Mo edge on one side and pristine ZZ-S edge on the other side.

1.3 For armchair (AC) edges, symmetric nanoribbons were used directly (Figure S3) to calculate the edge formation energy. The other reconstructed AC edges were calculated based on nanoribbons with one pristine AC edge.

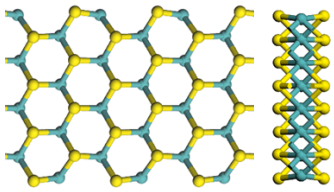

Figure S3. The optimized nanoribbon with pristine AC edge one two sides.

2. On Au (111) surface:

2.1 Since pristine Mo edges are unstable (Mo atom would extract Au atoms on the surface, Figure S9), Mo-III triangular clusters were built to calculate the formation

energy with considering vdW interactions (Figure S4):

$$E_{Mo-III\ on\ Au} = \frac{E_1 - E_2 - \Delta E_{vdW} - \Delta N_{Mo}\mu_{Mo} - \Delta N_S\mu_S}{3(l_1 - l_2)} \#(3)$$

where E_1 and E_2 are the total energies of the two triangular clusters on Au (111) surface, ΔE_{vdw} denotes the energy difference in the vdW interaction between the two triangular clusters with Au (111) surface.

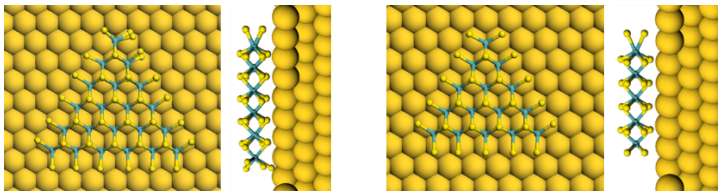

Figure S4. Two optimized triangular MoS_2 domains on Au (111) surface with only Mo-III edge.

The vdW interaction can be calculated (Figure S5):

$$E_{vdw} = (E_{total} - E_{Au} - E_{MoS_2})/N \#(4)$$

where N represents the number of MoS_2 units (one unit is equal to 1Mo+2S) incorporated in the MoS_2 monolayer sheet in Figure S5.

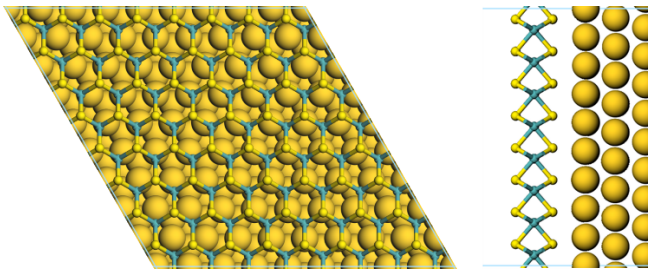

Figure S5. Periodic computational model for calculating vdW interactions.

2.2 Nanoribbons with ZZ-Mo edge and ZZ-S edges were used to calculate the

formation energy of ZZ-S edges on Au (111) surface (Figure S6):

$$E_{S\ edge\ on\ Au} = \frac{E_{total} - E_{Au} - \Delta N_{Mo}\mu_{Mo} - \Delta N_S\mu_S - E_{vdW} \times N - E_{Mo-III\ on\ Au} \times L}{L} \#(5)$$

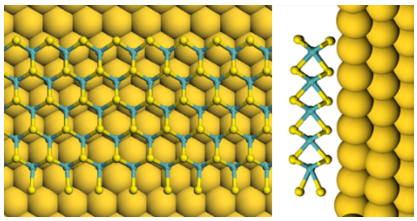

Figure S6. The optimized nanoribbon on Au (111) surface with Mo-III edge on one side and pristine ZZ-S edge on the other side.

2.3 For AC edges, similarly, symmetric nanoribbons were used directly (Figure S7) to calculate the edge formation energy.

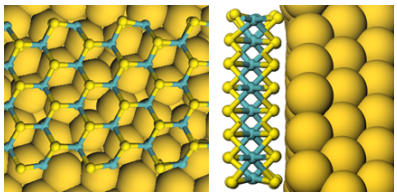

Figure S7. The optimized nanoribbon on Au (111) surface with pristine AC edge on two sides.

3. All edge structures are shown below in Figures S8-S14.

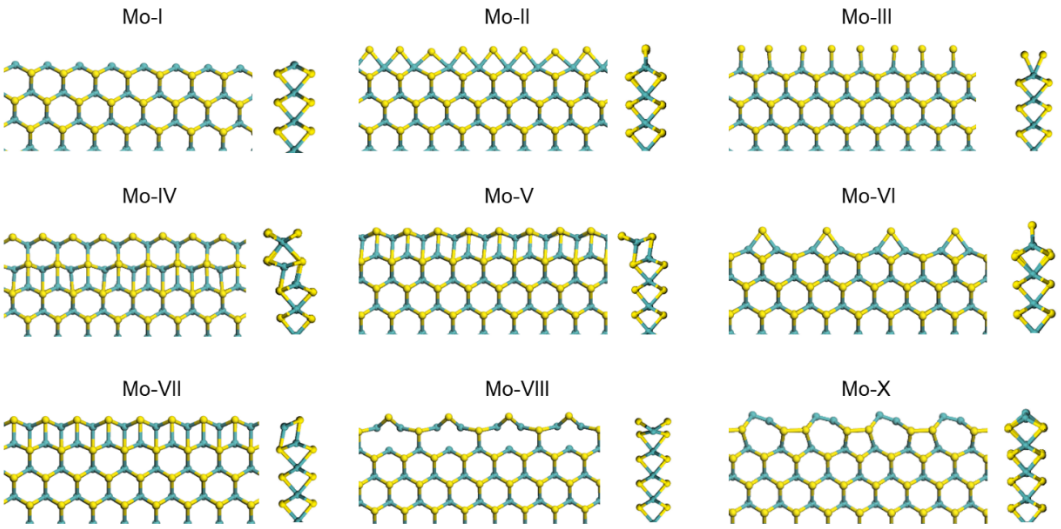

Figure S8. Optimized ZZ-Mo edges in vacuum. Front and sides views are given.

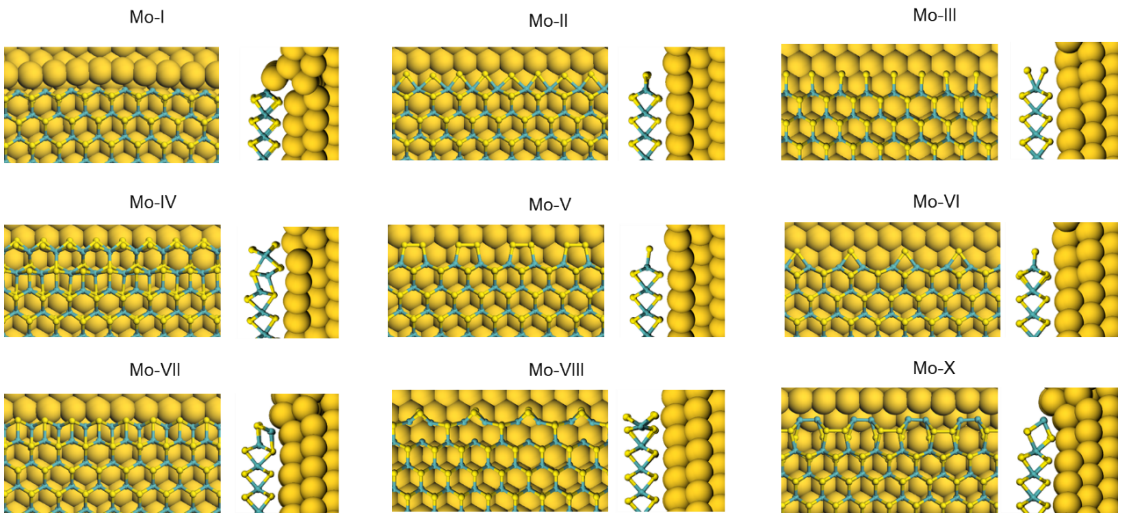

Figure S9. Optimized ZZ-Mo edges on Au (111) surface. Front and sides views are given.

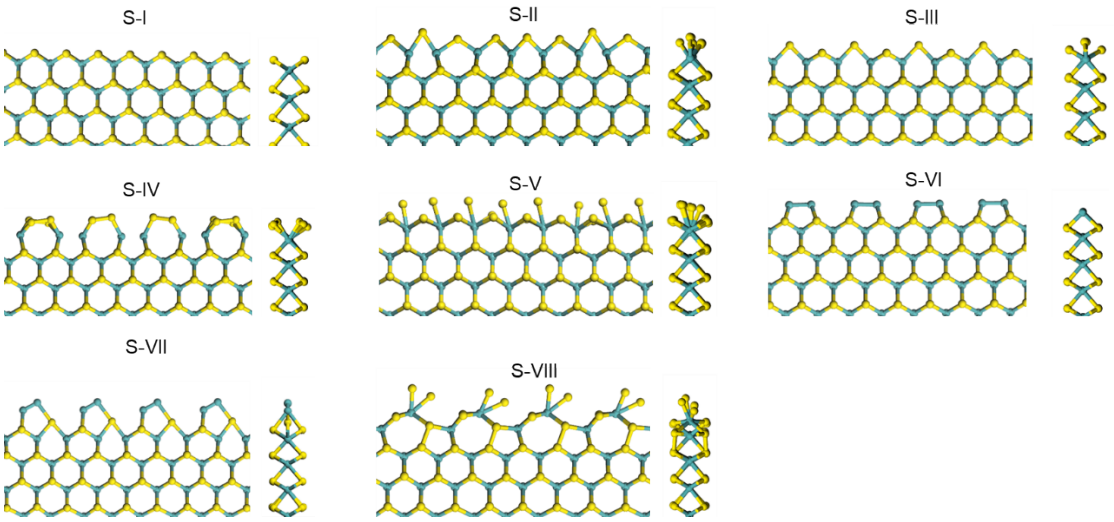

Figure S10. Optimized ZZ-S edges in vacuum. Front and sides views are given.

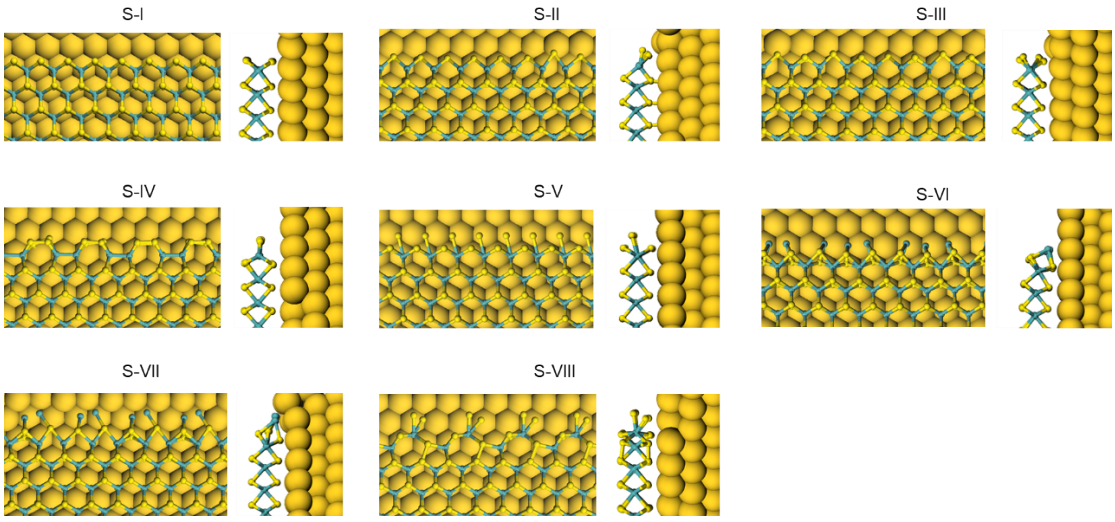

Figure S11. Optimized ZZ-S edges on Au (111) surface. Front and sides views are given.

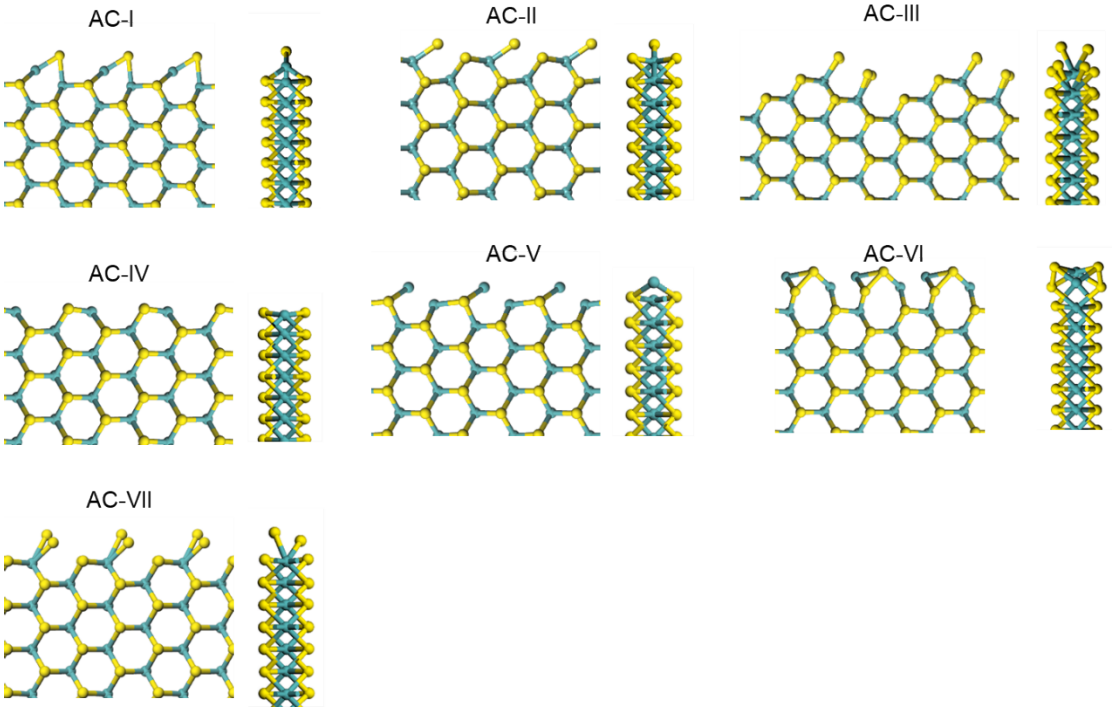

Figure S12. Optimized AC edges in vacuum. Front and sides views are given.

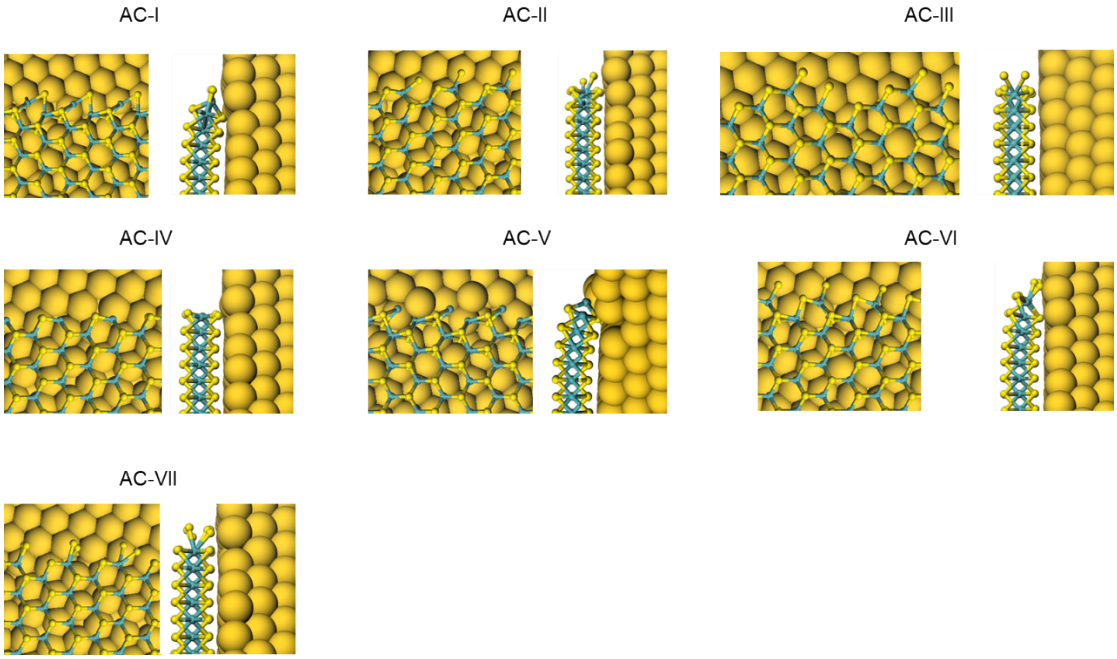

Figure S13. Optimized AC edges on Au (111) surface. Front and sides views are given.

4. The stability of Au-passivated edges.

Considering the strong interaction between Au and Mo atoms, the exposed Mo atoms at the edges are expected to be passivated by Au atoms from the Au(111) substrate. Accordingly, we examined the stability of Au-passivated edges for both ZZ-Mo edge (Mo-t edge) and AC edge (AC-t), as shown in Fig. S14. Although the results indicate that Au-passivated Mo edge is energetically favorable under Mo-rich conditions, it does not exhibit energetic advantages in S-rich environment. Since the CVD growth of MoS_2 for morphology control is generally conducted in S-rich conditions, Au-passivated edge structures are not considered in the subsequent calculations.

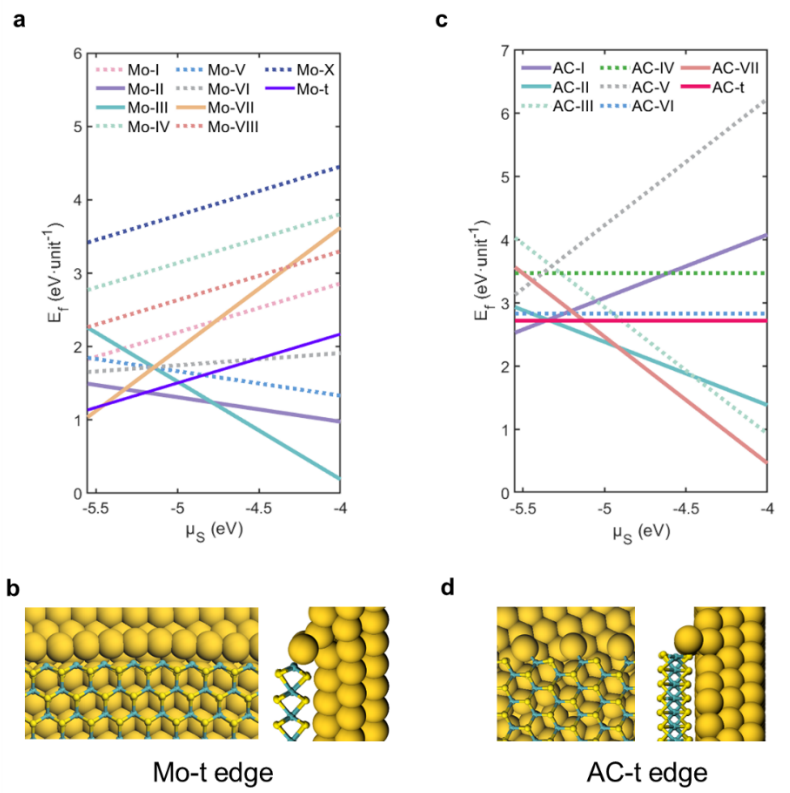

Figure S14. Thermodynamic exploration on the morphology of MoS_2 on the Au(111) surface. (a-b) Formation energies of various ZZ-Mo edges as a function of μ_S and ZZ-Mo edge passivated by Au atoms (Mo-t edge) on Au(111) surface. (c-d) Formation

energies of various AC edges as a function of μ_S and AC edge passivated by Au atoms (AC-t edge) on Au(111) surface.

5. Calculation of S chemical potential range

The chemical potential range of S captures the transition of the system from Mo-rich to S-rich conditions. In the S-rich environment, the chemical potential of S is referenced to an S_8 molecular crystal, which is obtained by $\mu_S = \frac{E_{S\ bulk}}{n_S}$. Similarly, in the Mo-rich environment, the chemical potential of Mo was determined using bulk Mo in its body-centered cubic (BCC) crystal structure as the reference, we got $\mu_{Mo} = \frac{E_{Mo\ bulk}}{n_{Mo}}$. The chemical potential of S then can be obtained based on $2\mu_S + \mu_{Mo} = \varepsilon_{MoS_2}$.

II. Thermodynamically preferred edge structures and Wulff construction for the equilibrium shape of MoS_2 under different μ_S.

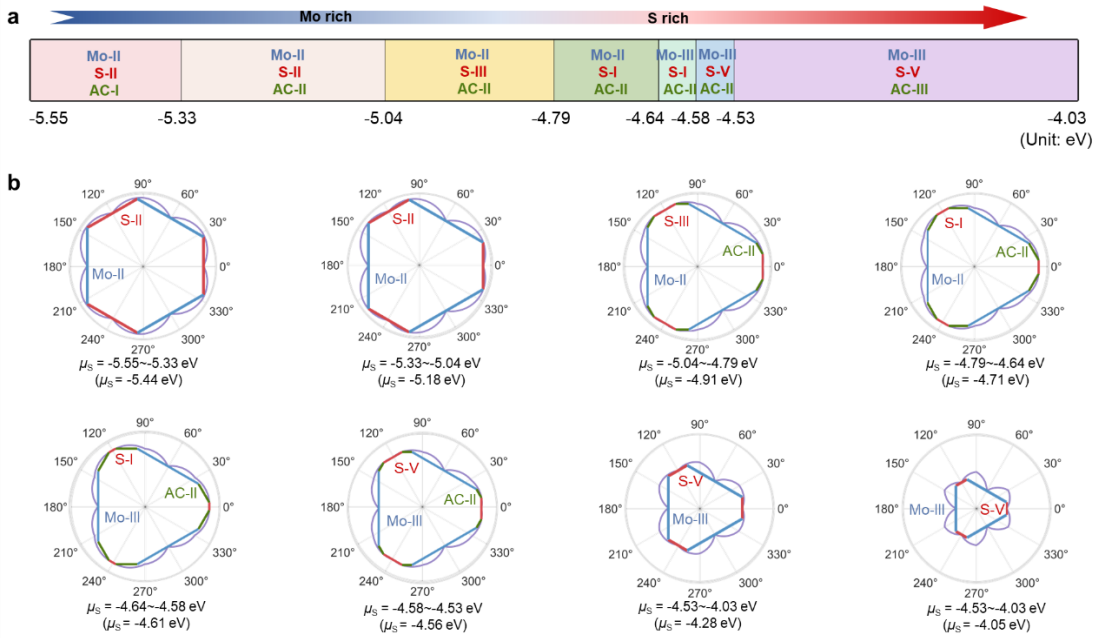

Figure S15. (a) Diagram of the most stable edges of MoS_2 at different μ_S ranges in vacuum. (b) Wulff construction for the equilibrium shape of MoS_2 domain at different μ_S during the entire process of the change of μ_S.

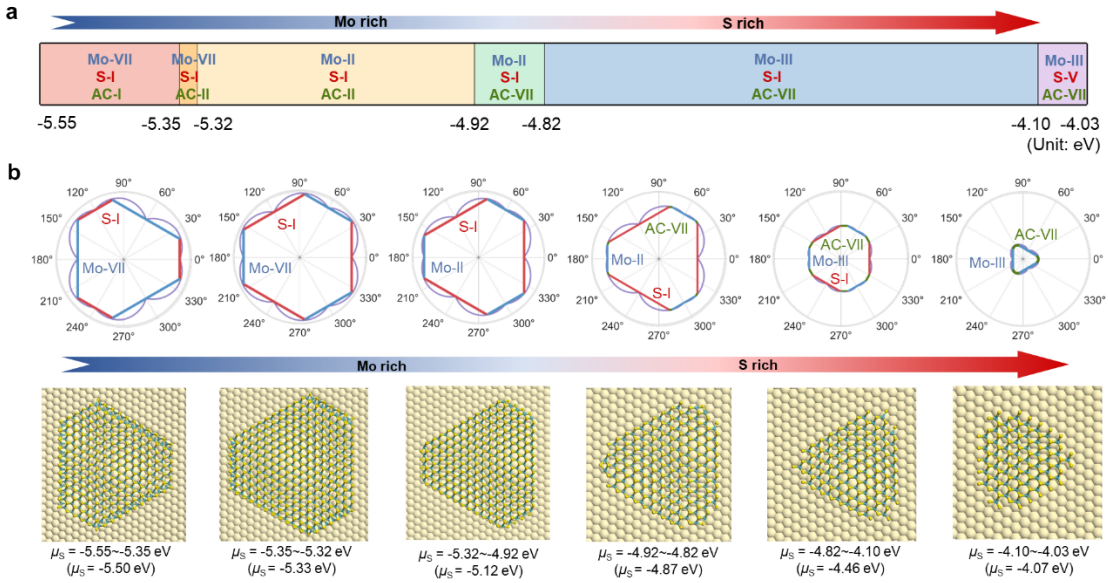

Figure S16. Diagram of the most stable edges of MoS_2 at different μ_S ranges on Au (111) surface. (b) Wulff construction and corresponding atomic configuration for the equilibrium shape of MoS_2 domain at different μ_S during the entire process of the change of μ_S.

III. Calculation of kinetic growth of MoS_2

We employ the kinetic Wulff construction to model the evolution of crystal morphology. During crystal growth, edges with different orientations propagating along their normal directions. Edges with higher growth rates tend to vanish over time, while those with slower velocities persist. As a result, the final crystal morphology is primarily governed by the slowest-growing edges, which ultimately define the overall shape of the crystal.

We computed the growth rates of the ZZ and AC edge as follows[1, 2]:

$$S_Z^{'}(\chi) = cos\chi - \sqrt{3}sin\chi \#(6)$$

$$S_A^{'}(\chi) = \begin{cases} 0 & \chi < \beta \\ \frac{5}{\sqrt{3}}sin\chi - cos\chi & \chi \geq \beta \end{cases} \#(7)$$

$$S_K^{'}(\chi) = \begin{cases} \frac{2}{\sqrt{3}}sin\chi & \chi < \beta \\ 2\sin\left(\frac{\pi}{6} - \chi\right) & \chi \geq \beta \end{cases} \#(8)$$

$$S_K(\chi) = e^{\frac{-E_Z}{kT}}\left[\left(1 + 2S_Z^{'}(\chi)e^{\frac{E_Z}{kT}} + \left(S_K^{'}(\chi)\right)^2 e^{\frac{2E_Z}{kT}}\right)^2 - 1\right] \#(9)$$

$$S_Z = S_Z^{'}(\chi) - \left(S_K(\chi) - S_K^{'}(\chi)\right) \#(10)$$

$$S_A = \begin{cases} 0 & \chi < \beta \\ S_A^{'}(\chi) - \left(2 \times S_K(\chi) - S_K^{'}(\chi) - S_Z^{'}(\chi)\right) & \chi \geq \beta \end{cases} \#(11)$$

$$\beta = arctan\frac{\sqrt{3}}{5} \#(12)$$

$S_K^{'}(\chi)$ is the intrinsic concentration of kink sites along arbitrary orientations, $S_K(\chi)$ is the corrected concentration of kink sites. $S_Z^{'}(\chi)$is the intrinsic concentration of ZZ sites, $S_Z$is the corrected concentration of ZZ sites. $S_A^{'}(\chi)$is the intrinsic concentration of AC sites, $S_A^{'}(\chi)$is the corrected concentration of AC sites. E_Z denotes the growth barrier of the ZZ edge. Therefore, the growth rate of MoS_2 edges along arbitrary orientations on the Au substrate can be expressed as:

$$R(\chi) \approx S_Z \times (e^{\left(-\frac{E_Z}{kT}\right)} + S_A \times e^{\left(-\frac{E_A}{kT}\right)} + S_K) \#(13)$$

where R represents the growth rate of edges along arbitrary orientations, E_A denotes the growth barrier of the AC edge. As shown in Figure S16, the growth rate of the AC edge is much greater than that of the ZZ edge. In the subsequent exploration of the morphology of MoS_2 crystal domain dynamic growth, the ZZ edge determines the final morphology of the crystal domain. Considering the E_A of AC edges is very small or negative, we neglect the $S_A \times e^{\left(-\frac{E_A}{kT}\right)}$ term in our final calculations of growth rate of ZZ edges, hence:

$$R(\chi) \approx S_Z \times (e^{\left(-\frac{E_Z}{kT}\right)} + S_K) \#(14)$$

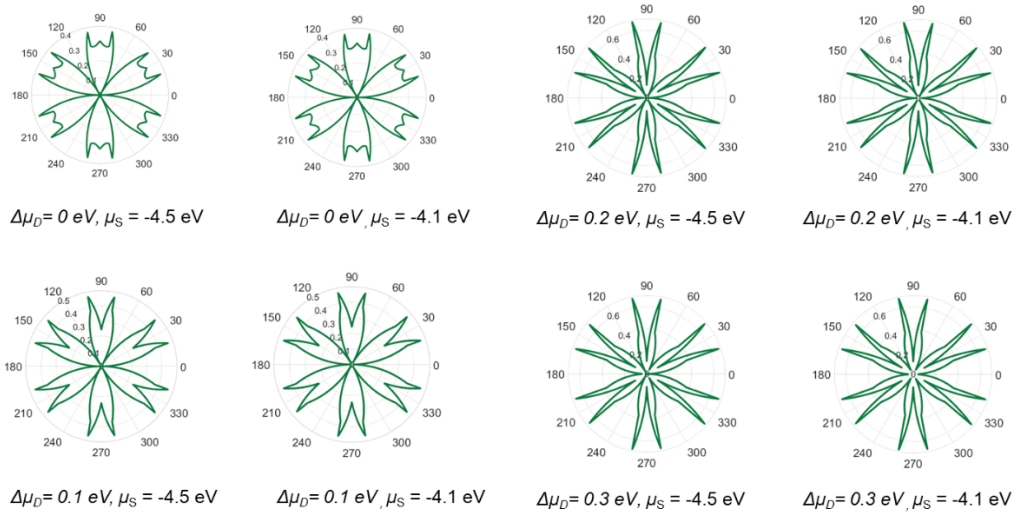

Figure S17. Direction-dependent edge growth rates.

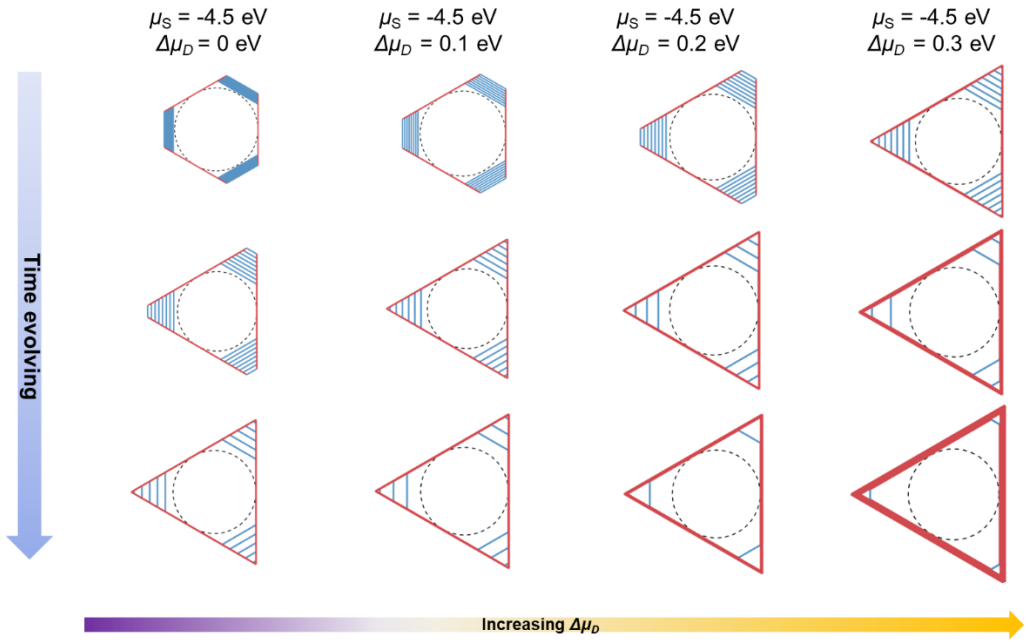

Figure S18. The site-dependent kinetic Wulff construction models of MoS_2 at μ_S = -4.5 eV and $\Delta\mu_D$ = 0, 0.1, 0.2 and 0.3 eV. The red line represents the S-I edge, while the blue line denotes the Mo-III edge.

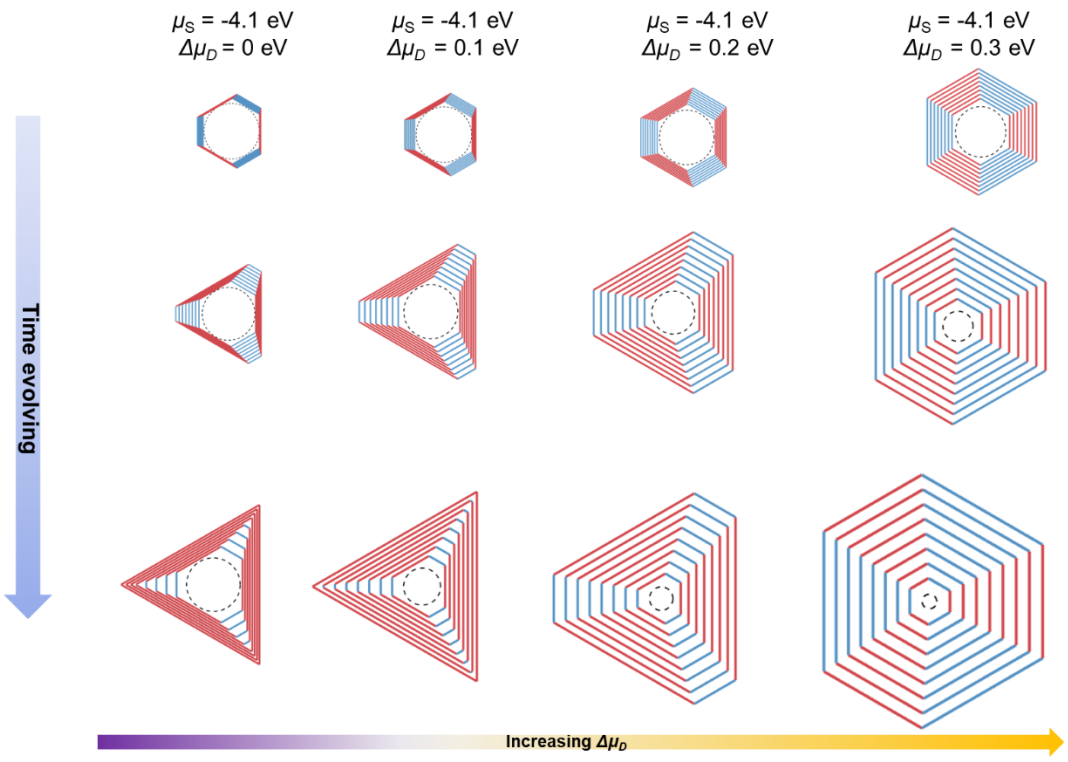

Figure S19. The site-dependent kinetic Wulff construction models of MoS_2 at μ_S = -4.1 eV and $\Delta\mu_D$ = 0, 0.1, 0.2 and 0.3 eV. The red line represents the S-I edge, while the blue line denotes the Mo-III edge.

IV. Exploration of moiré superstructure-dependent growth behaviors of MoS_2

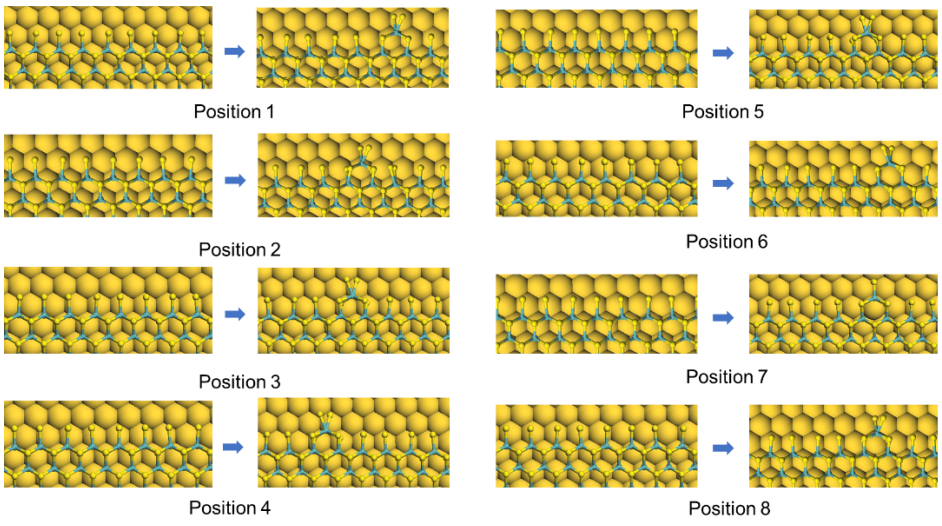

Figure S20. The models of Mo-III edge growth for MoS_2 on Au (111) surface.

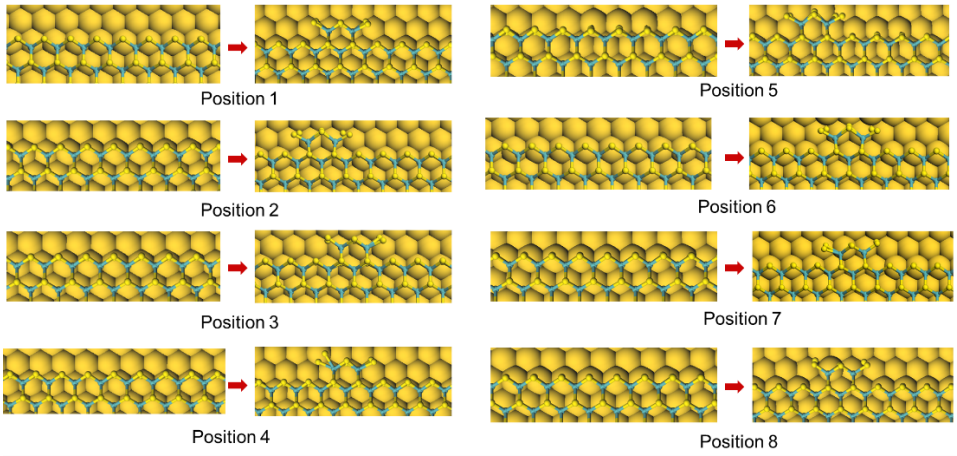

Figure S21. The models of S-I edge growth for MoS_2 on Au (111) surface.

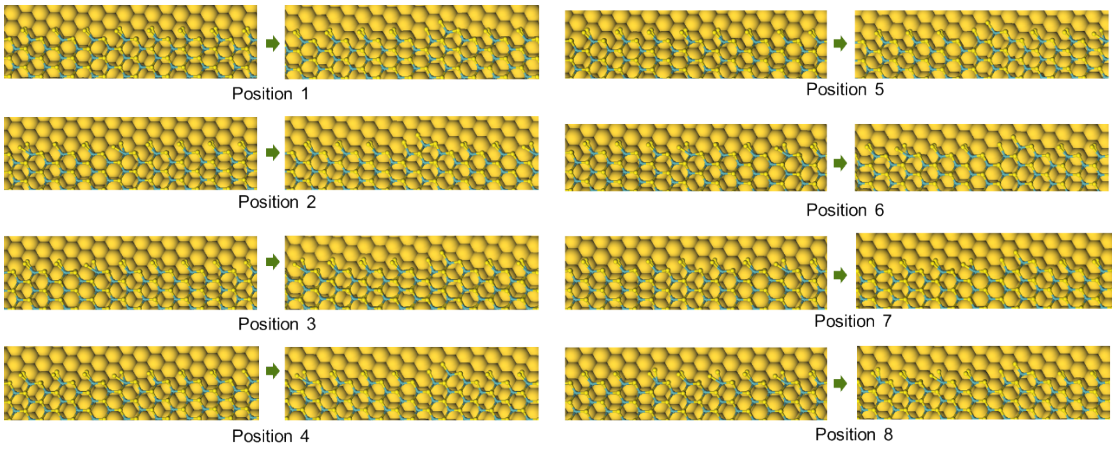

Figure S22. The models of AC-VII edge growth for MoS_2 on Au (111) surface.

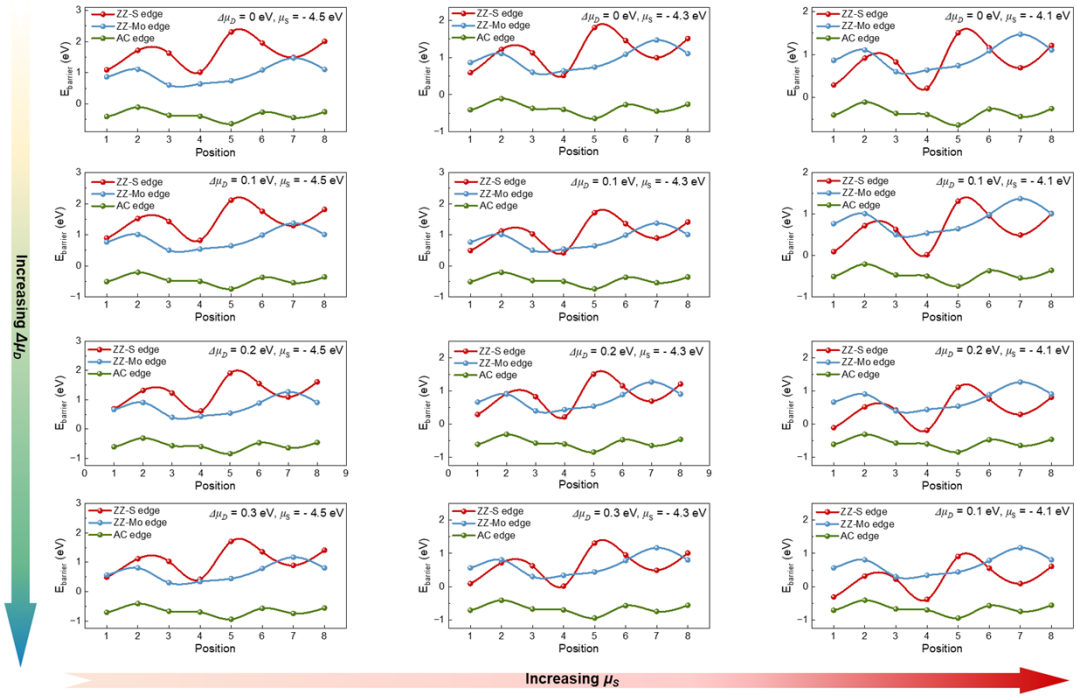

Figure S23. Growth barrier profiles of Mo-III edge, S-I edge and AC- VII edge at $\Delta\mu_D$ = 0, 0.1, 0.2 and 0.3 eV under different μ_S.

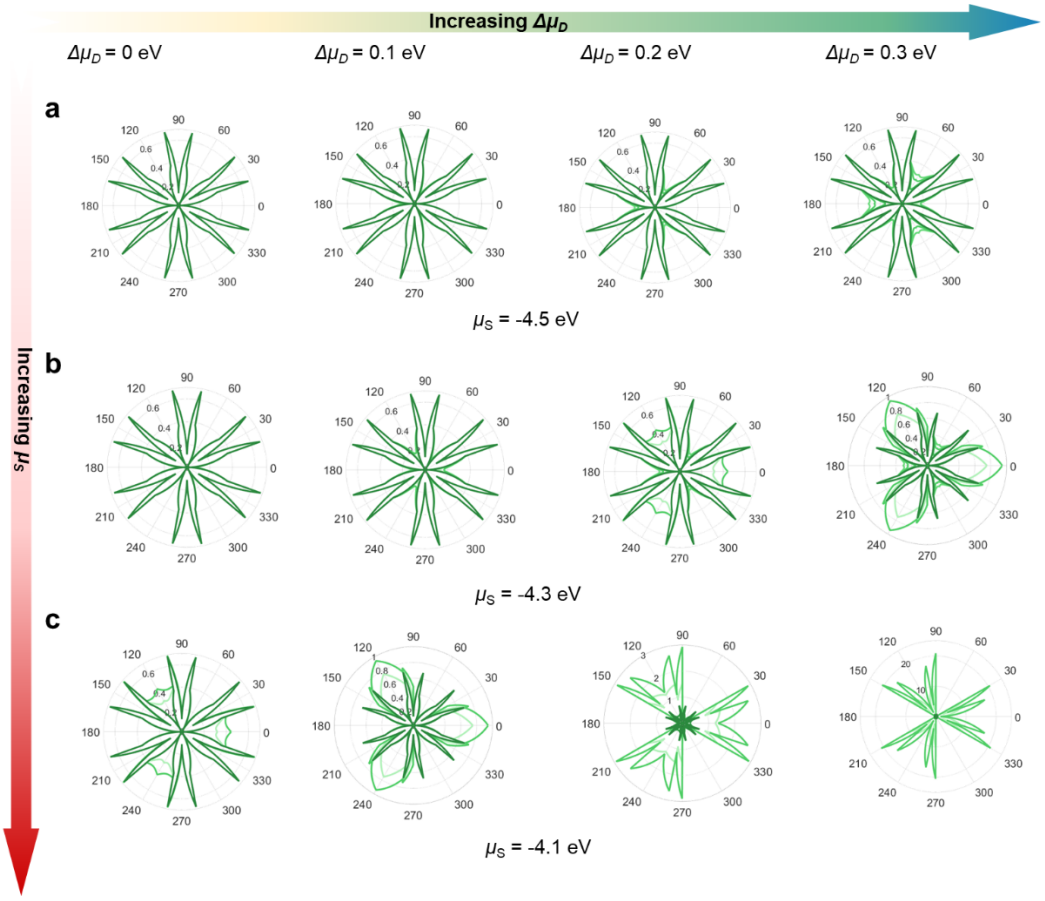

Figure S24. Direction-dependent edge growth rates. Different colored lines indicate the rates at different positions.

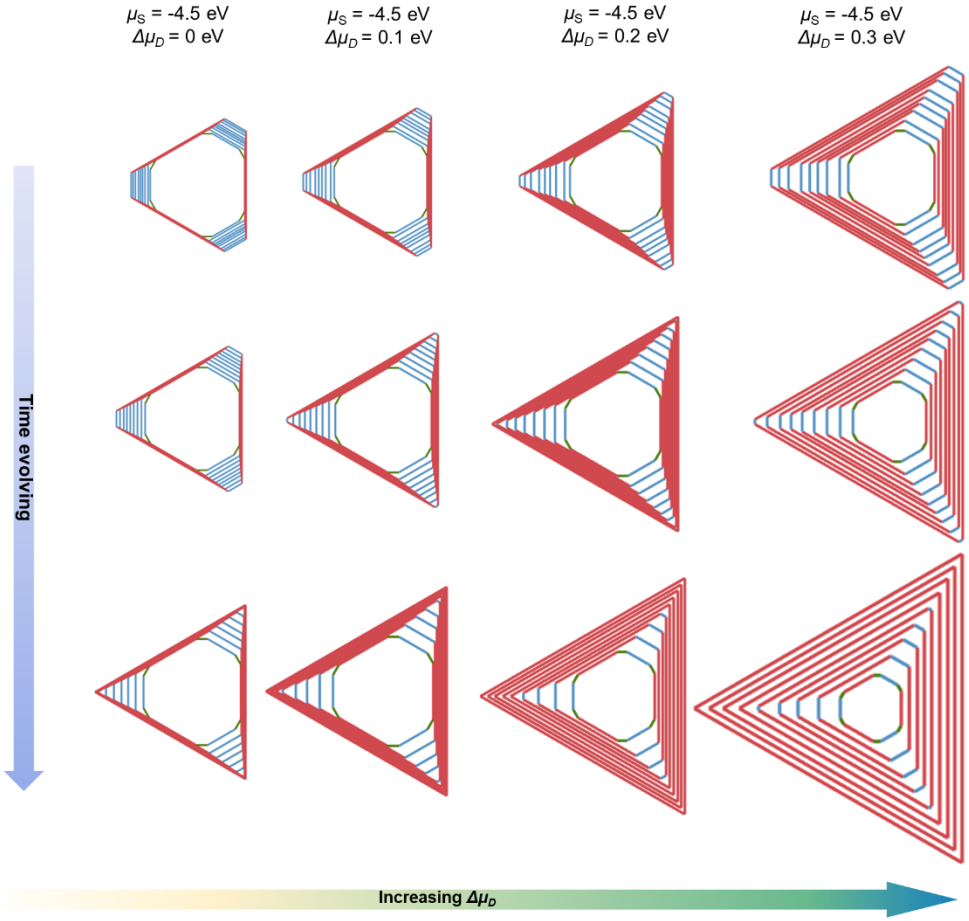

Figure S25. The moiré superstructure-dependent kinetic Wulff construction models of MoS_2 at μ_S = -4.5 eV and $\Delta\mu_D$ = 0, 0.1, 0.2 and 0.3 eV. The red line represents the S-I edge, while the blue line denotes the Mo-III edge.

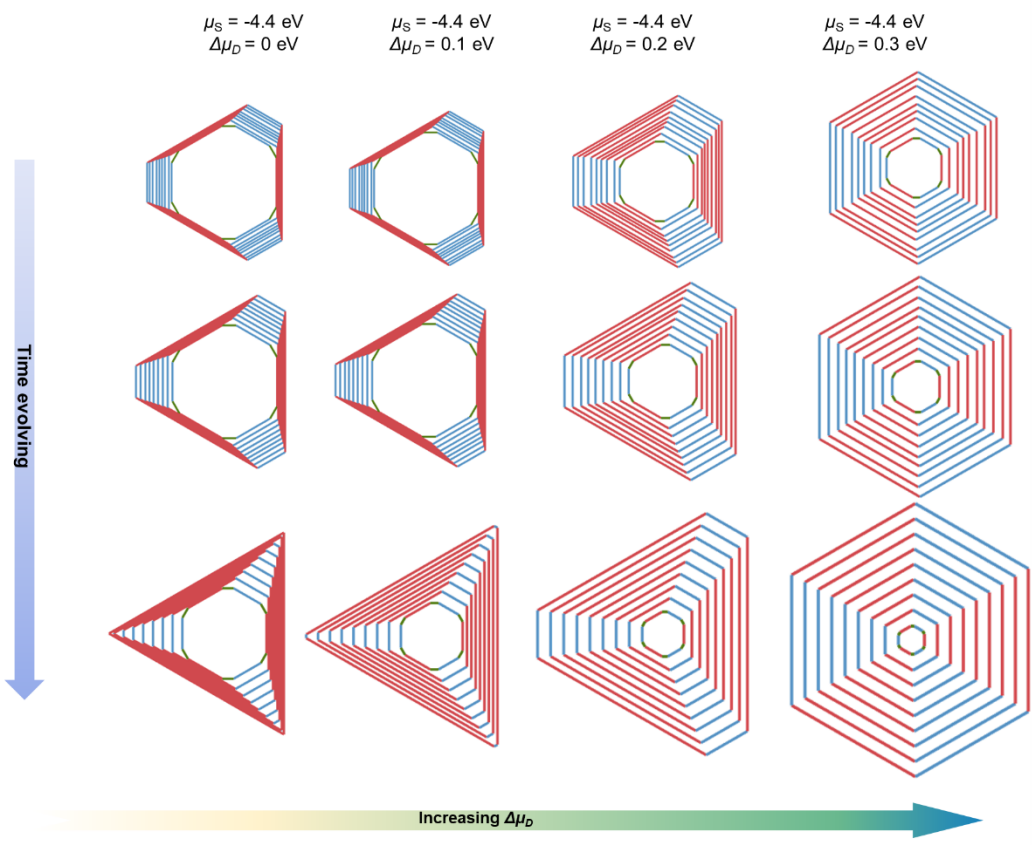

Figure S26. The moiré superstructure-dependent kinetic Wulff construction models of MoS_2 at μ_S = -4.4 eV and $\Delta\mu_D$ = 0, 0.1, 0.2 and 0.3 eV. The red line represents the S-I edge, while the blue line denotes the Mo-III edge.

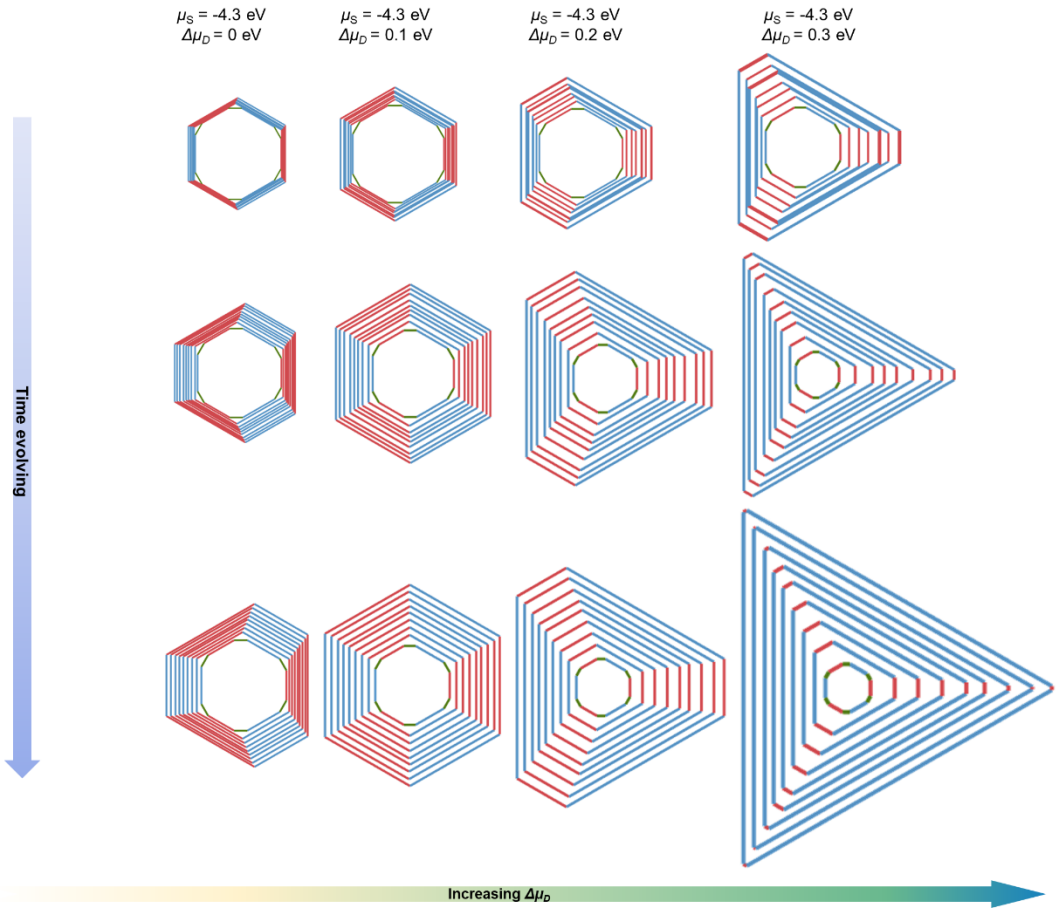

Figure S27. The moiré superstructure-dependent kinetic Wulff construction models of MoS_2 at μ_S = -4.3 eV and $\Delta\mu_D$ = 0, 0.1, 0.2 and 0.3 eV. The red line represents the S-I edge, while the blue line denotes the Mo-III edge.

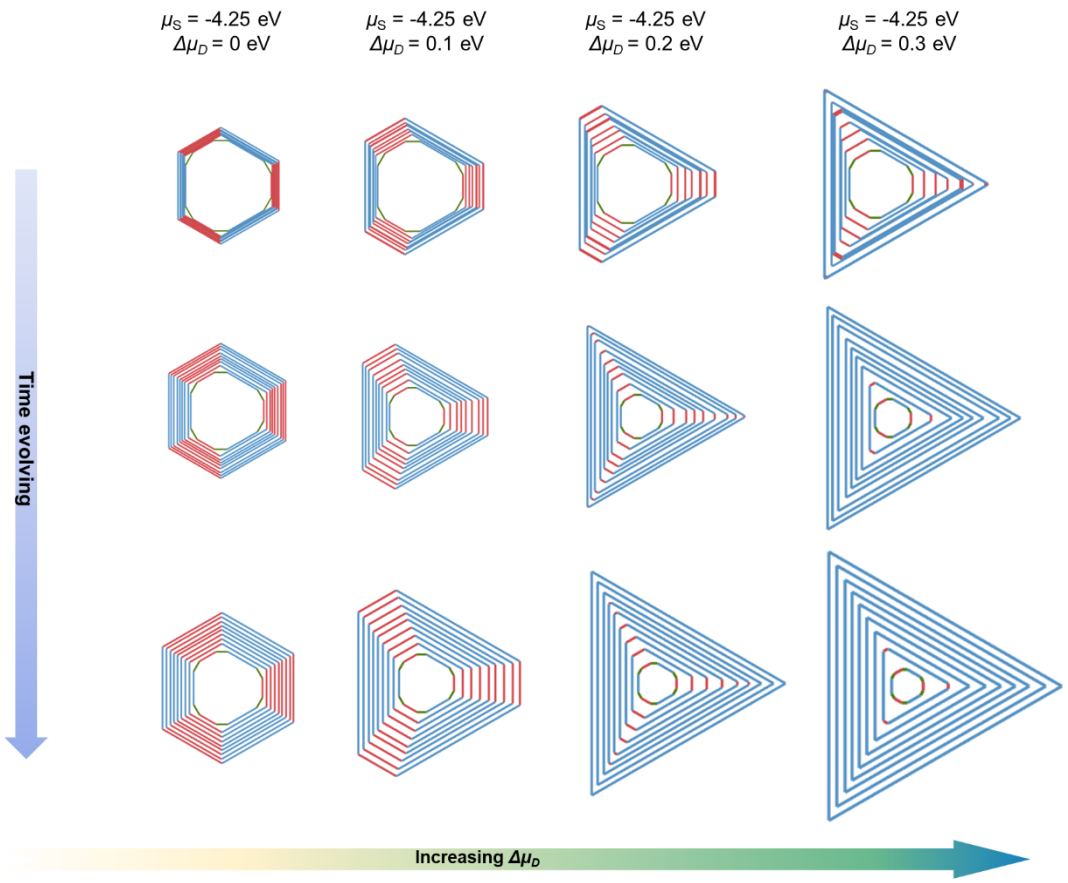

Figure S28. The moiré superstructure-dependent kinetic Wulff construction models of MoS_2 at μ_S = -4.25 eV and $\Delta\mu_D$ = 0, 0.1, 0.2 and 0.3 eV. The red line represents the S-I edge, while the blue line denotes the Mo-III edge.

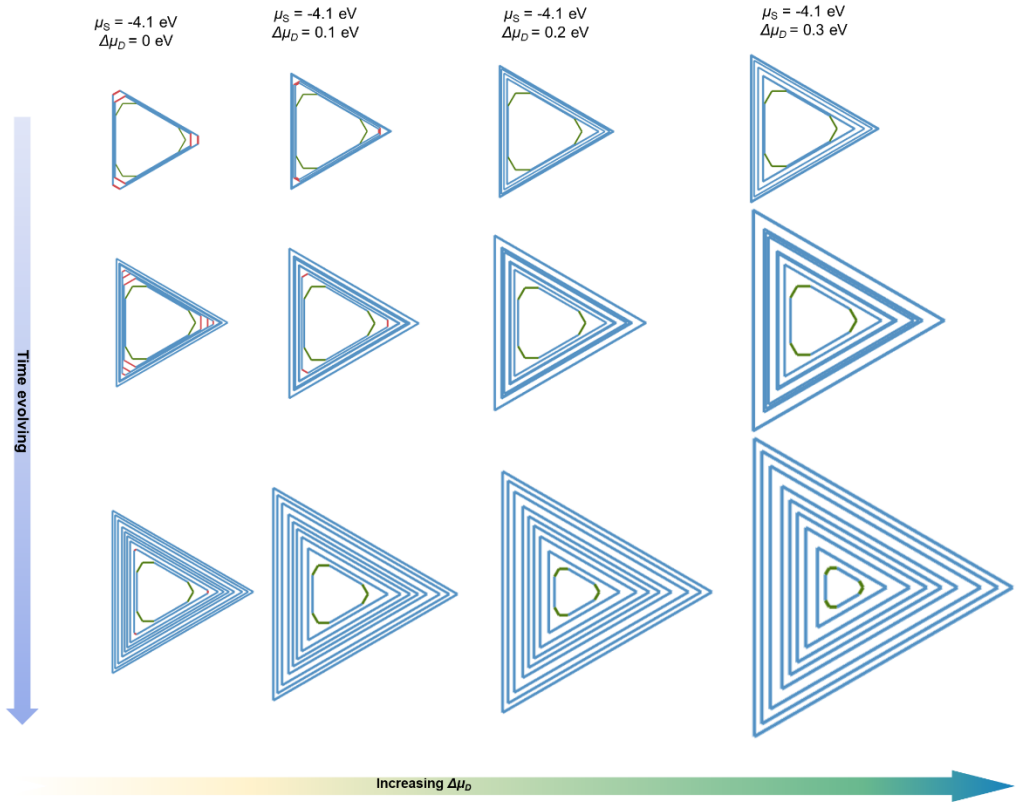

Figure S29.The moiré superstructure-dependent kinetic Wulff construction models of MoS_2 at μ_S = -4.1 eV and $\Delta\mu_D$ = 0, 0.1, 0.2 and 0.3 eV. The red line represents the S-I edge, while the blue line denotes the Mo-III edge.

V. Investigation of orientations of MoS_2 domains with different morphologies and edge structures on Au (111) surface

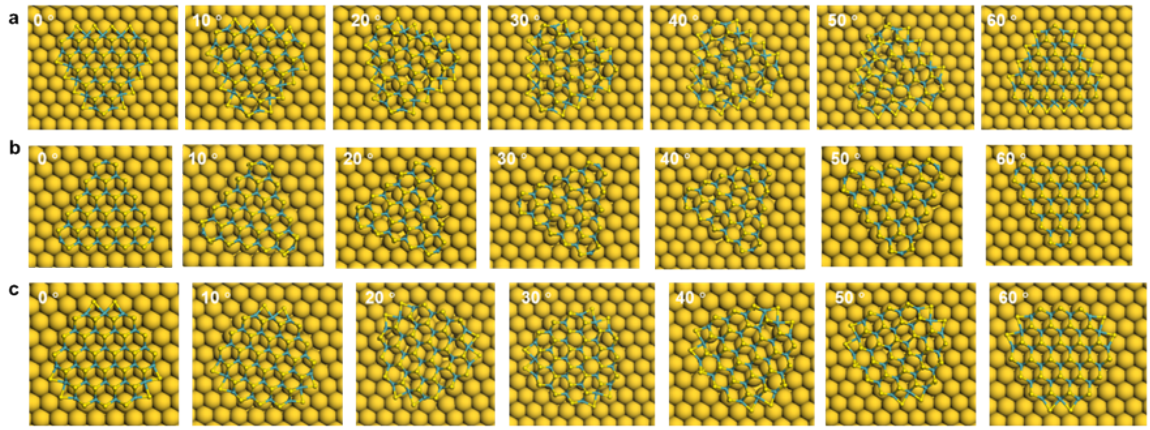

Figure S30. Structural diagrams of triangular domains enclosed by ZZ-Mo edges, triangular domains enclosed by ZZ-S edges, and hexagonal domains alternately formed by ZZ-Mo and ZZ-S edges on the Au (111) surface at different orientations.

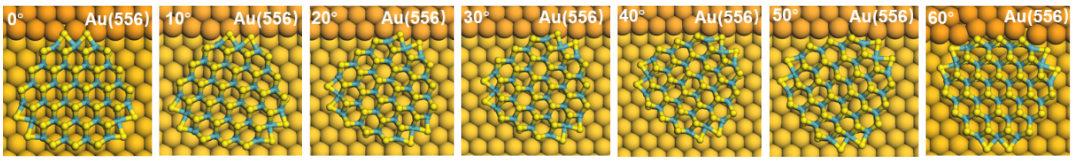

Figure S31. Structural diagrams of hexagonal domains alternately formed by ZZ-Mo and ZZ-S edges near the step on the Au (111) surface at different orientations. Atoms in orange and yellow colors represent the Au atoms of step and terrace, respectively.

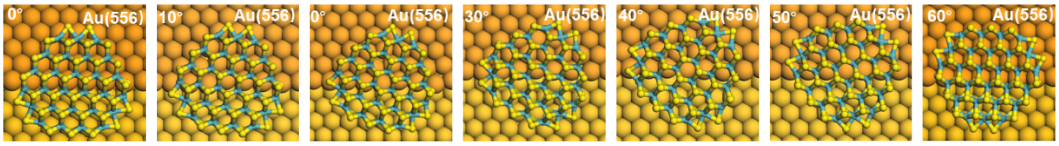

Figure S32. Structural diagrams of hexagonal domains alternately formed by ZZ-Mo and ZZ-S edges over the step on the Au (111) surface at different orientations. Atoms in orange and yellow colors represent the Au atoms of step and terrace, respectively.

VI. Reference

1.T. Maa, W. Rena, X. Zhangb, Z. Liua, Y. Gaoa, L.-C. Yina, X.-L. Maa, F. Ding and H.-M. Chenga, *Proc. Natl. Acad. Sci. U.S.A.*, 2013, **110**, 20386-20391.

2.V. I. Artyukhova, Y. Liua and B. I. Yakobson, *Proc. Natl. Acad. Sci. U.S.A.*, 2012, **109**, 15136–15140.